Object registration techniques for 3D particle tracking

Hendriksen, L. A.; Sciacchitano, A.; Scarano, F.

DOI
10.1088/1361-6501/ad715c

Publication date
2024

Document Version
Final published version

Published in
Measurement Science and Technology

OPEN ACCESS
IOP Publishing
Measurement Science and Technology
Meas. Sci. Technol. **35** (2024) 125202 (16pp)
https://doi.org/10.1088/1361-6501/ad715c

Object registration techniques for 3D particle tracking

L A Hendriksen*, **A Sciacchitano** and **F Scarano**

Aerospace Engineering Department, TU Delft, Delft, The Netherlands

E-mail: L.A.Hendriksen@tudelft.nl

Received 16 May 2024, revised 24 July 2024
Accepted for publication 20 August 2024
Published 12 September 2024

Abstract

Image based three-dimensional (3D) particle tracking is currently the most widely used technique for volumetric velocity measurements. Inspecting the flow-field around an object is however, hampered by the latter, obstructing the view across it. In this study, the problem of measurement limitations due to the above is addressed. The present work builds upon the recent proposal from Wieneke and Rockstroh (2024 *Meas. Sci. Technol.* **35** 055303), whereby the information of the occluded lines of sight can be incorporated into the particle tracking algorithm. The approach, however, necessitates methods that accurately evaluate the shape and position of the object within the measurement domain. Methods of object marking and the following 3D registration of a digital object model (CAD) are discussed. For the latter, the iterative closest point registration algorithm is adopted. The accuracy of object registration is evaluated by means of experiments, where marking approaches that include physical and optically projected markers are discussed and compared. Three objects with growing level of geometrical complexity are considered: a cube, a truncated wing and a scaled model of a sport cyclist. The registered CAD representations of the physical objects are included in aerodynamic experiments, and the flow field is measured by means of large-scale particle tracking using helium filled soap bubbles. Results indicate that object registration enables a correct reconstruction of flow tracers within regions otherwise affected by domain clipping as a consequence of obstructed camera lines-of-sight. Finally, the combined visualization of the object and the surrounding flow pattern offers means of insightful data inspection and interpretation, along with posing a basis for particle image velocimetry data assimilation at the fluid-solid interface.

Keywords: LPT, STB, 3D-PIV, HFSB, Tomo PIV, ICP

1. Introduction

Three-dimensional (3D) measurements of fluid flow velocity are currently performed with particle image velocimetry (PIV) techniques that have evolved from the tomographic principle (Elsinga *et al* 2006) towards individual particle tracking (Schröder and Schanz 2023). Compared to tomographic PIV, particle tracking offers measurements with a higher dynamic range, lower data storage requirements and decreased computational time. Recent particle tracking experiments have reached measurement volumes of up to cubic meter scales (Jux *et al* 2018, Schröder *et al* 2022). Upscaling of 3D experiments in air flows have been enabled with the introduction of helium filled soap bubbles (HFSB) (Bosbach *et al* 2009) providing orders of magnitude higher light scattering compared to micron-sized droplets (Grille Guerra *et al* 2024). The developments of 3D particle tracking have been further facilitated by

* Author to whom any correspondence should be addressed.

advancements in system calibration (Wieneke 2008), accurate particle image triangulation algorithms (Wieneke 2013) and the efficient and robust Lagrangian particle tracking algorithm *shake-the-box* (STB, Schanz *et al* 2016). Despite the above advancements, most particle tracking experiments focus on simplified geometrical conditions such as boundary layers, free wakes or cavities (Schröder and Schanz 2023). When an object is immersed in the flow, the measurement is hampered in the regions where the view or the illumination is blocked by the object. Hysa *et al* (2023) have recently discussed the problem of estimating such volume losses when using a multi-camera 3D-PIV system, as a result of shadows and occlusion of camera views generated by one or more objects within the measurement volume. The erosion of the measurement volume caused by shadows is simply solved using two or more directions of illumination. In contrast, the problem of camera occlusion is of more complex nature as it entails the logics of 3D particle detection from a multitude of simultaneous views. The proposed practical solution has been that of partitioning the imaging system into multiple, independent subsystems (Hysa *et al* 2023). Such approach showed benefits in terms of increased measurement coverage over the domain of interest, at the cost however, of a larger amount of ghost particles (Elsinga *et al* 2011).

The recent work of Wieneke and Rockstroh (2024) proposes an algorithm that circumvents the requirement of a global (i.e. by all cameras) simultaneous view at every point of the measurement domain. The algorithm, however, requires the object position to be known a-priori, or experimentally determined, which opens up to the scope of the current work. Furthermore, the accurate determination of the object position within the measurement volume is beneficial for a number of reasons: it facilitates more accurate evaluation of near-surface flow properties such as pressure and skin friction (Depardon *et al* 2005); it benefits data reduction, visualization and assimilation techniques through an accurate description of the fluid-solid interface (Cakir *et al* 2022).

Approaches to 3D object position and orientation determination have been extensively studied in various domains, including medical imaging, machine vision and urban navigation for example (Saiti and Theoharis 2020). The problem has been occasionally addressed in the PIV community. For instance Adhikari and Longmire (2012) proposed the *visual-hull* technique, whereby object silhouettes appearing within the camera images of a multi-camera setup are back-projected into physical space. Their intersection yields an approximate 3D hull, which encompasses the object within the measurement volume. This technique is applicable to moving objects and complex shapes, making it a suited technique for flow measurements involving living animals as exemplified by Adhikari and Longmire (2013), Mendelson and Techet (2018) and Langley *et al* (2014). The visual-hull technique, however, suffers from the inability to detect concave regions and relies on edge-detection, with specific requirements on the object appearance- and illumination conditions, which often conflict with the need to detect the light scattered by the tracer particles in front of the object.

In Jux *et al* (2021), an *in-situ* approach to object surface reconstruction solely based on flow tracers is introduced, where the void in particle distributions is associated with the presence of a solid object. The method reconstructs satisfactorily simple, smooth objects but it requires a high particle concentration to reconstruct complex shapes or to deal with sharp edges.

In aircraft aerodynamics, studies dealing with object motion and deformation have made use of surface markers (Liu *et al* 2012) with most frequent focus on structural deflection monitoring and not on the evaluation of fluid motion. Markers, either printed or projected onto the surface are among the most practiced methods (Pappa *et al* 2003). The use of a speckle pattern enables a dense and more accurate determination of object position and deformation, according to the digital image correlation (DIC) method (Pan 2018). More recently, the DIC technique has been combined with image-based volumetric flow measurements in the context of fluid structure interaction in Acher *et al* (2019) and Zhang *et al* (2019) who adopted separate measurement systems to determine simultaneously the structural behavior of an aerodynamic test object and the flow around it. Measuring both structure and fluid using a single measurement setup has been demonstrated by e.g. Jeon and Sung (2012) when the surface markers can be separated from the flow markers.

Many advancements have been obtained within the European HOMER (Holistic Optical Metrology for Aero-Elastic Research) project. The work by Mitrotta *et al* (2022) uses the STB algorithm for simultaneous measurements of retro-reflective surface markers and HFSB for the air motion. Mertens *et al* (2023) applied a similar approach to estimate structural-, inertial- and aerodynamic forces on a flexible wing solely from optical measurements. Obtaining an estimate of a continuously deforming elastic object from discrete points was achieved using polynomial functions that fit across the positions of few markers printed on the surface. The method was demonstrated to reconstruct the motion of a thin, flexible sheet subject to the Kármán wake past a circular cylinder (Saiz *et al* 2022). In some cases, direct tessellation of measured markers can be adopted, provided that their spatial density suffices (Jeon and Sung 2012).

The current work examines the process of object registration in 3D-PIV experiments, where a single set of cameras are used to render simultaneously the 3D velocity field along with the object position, with the aim of enhancing and simplifying the use of multi-camera systems for 3D aerodynamic experiments around complex objects. The study discusses first the problem of object registration, based upon the principles of the iterative closest point (ICP) algorithm (Besl and McKay 1992). Different approaches to object marking are examined and compared by means of laboratory experiments in terms of model surface coverage, registration accuracy and practicality. Furthermore, the feasibility of object registration for accurate particle reconstruction and data interpretability (in presence of object induced camera occlusion) for 3D-PIV are illustrated presenting three flow experiments that involve models of increasing geometrical complexity.

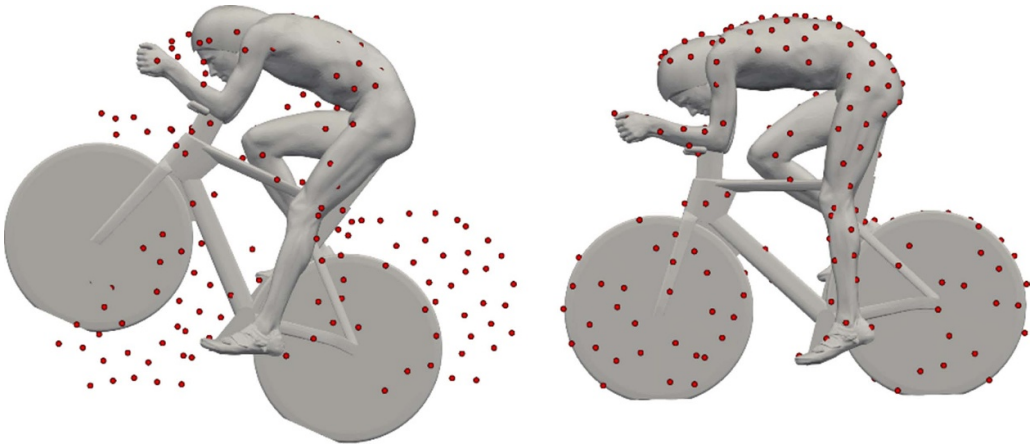

Figure 1. Illustration of the initial and final position of the cyclist CAD model registration based on experimental pointwise surface measurements of the marked object (red points).

2. ICP algorithm

The alignment of a 3D CAD model with the measured views of the corresponding object placed in the physical space and observed from several views is known as 3D object registration. Such task is frequently encountered in the field of computer vision (Saiti and Theoharis 2020). In 3D-PIV systems, object registration becomes necessary to identify regions of shadow and (partial) camera occlusion, which affect particle illumination and reconstruction. When the geometry of the object is known a-priori (e.g. most commonly as a CAD model used for manufacturing) the registration problem translates into the search for a transformation (translation and rotation) that brings the CAD model to accurately overlap with the object placed in physical space. Object registration comprises three steps: (1) the position of the CAD model is initialised (initial guess); (2) the disparity between model position and the actual object is estimated through an error metric; (3) a transformation is found such that the aforementioned error metric is minimized. An example of a CAD model (grey-shaded geometry) before and after being registered to a set of points (red dots) is shown in figure 1.

A commonly used registration algorithm is the ICP (Besl and McKay 1992), because of its relative simplicity and efficient implementations in open source programming libraries (Zhou *et al* 2018). The working principle of two variants of this algorithm for CAD model registration are illustrated in figure 2.

The ICP algorithm making use of a point-to-point error metric (figure 2, left) relies upon the assumption that the object is marked at prescribed locations on its surface (see section 3.1 for object marking techniques), for instance during manufacturing. The markers' coordinates are collected as the *target* point cloud $\boldsymbol{t}$. Correspondingly, the CAD model includes a set of points (virtual markers) referred to as the *source* point cloud $\boldsymbol{s}$. Starting from an initial guess, the ICP algorithm iterates over three steps: selection, matching and minimization (Rusinkiewicz and Levoy 2001). In the selection step, a search radius r_s is defined which determines the maximum distance a target point in $\boldsymbol{t}$ is allowed to search for a source point in $\boldsymbol{s}$. Large search radii improve the chance of matching, but make the process more prone to finding erroneous alignments. A (too) small search radius instead, improves convergence of the registration, at the risk however of discarding many valid points (the algorithm becomes 'short sighted', Segal *et al* 2009). In the matching step, target points are corresponded with their closest source point within the search radius. The established set of corresponding pairs is referred to as the correspondence set $\boldsymbol{K}$. A rigid body transformation matrix $\boldsymbol{M}$ is found, under which the following error metric $\epsilon(\boldsymbol{M})$ is minimized,

$$\varepsilon(\boldsymbol{M}) = \sum_{(s,t\in K)} ||\boldsymbol{M}\boldsymbol{s} - \boldsymbol{t}||^2. \tag{1}$$

The three steps are repeated until convergence. Since this involves direct minimization over the distance between corresponding point pairs, it is referred to as point-to-point ICP. In many applications however, as introduced in section 3.2, the application of surface markers at prescribed locations on an object is not practical. In these circumstances the so-called point-to-plane ICP variant (Chen and Medioni 1992) is more generally applicable (Pomerleau *et al* 2013). Point-to-plane ICP follows the same three steps, with some slight differences explained below and represented in figure 2-right.

Identical to point-to-point ICP, the registration is initialised from an initial guess of the CAD model position with respect to the estimated object position. A search radius is defined which allows the target points to find parts of the CAD model that lie within this distance. For each target point, the closest point on the CAD model surface (within the search radius) is computed and referred to as a source point. These source and target points form the correspondence set $\boldsymbol{K}$. Instead of using direct point-to-point distances for error metric minimization, the rigid transformation $\boldsymbol{M}$ aims at minimizing the distance $\boldsymbol{d_n}$ between the target points and the local tangent planes of

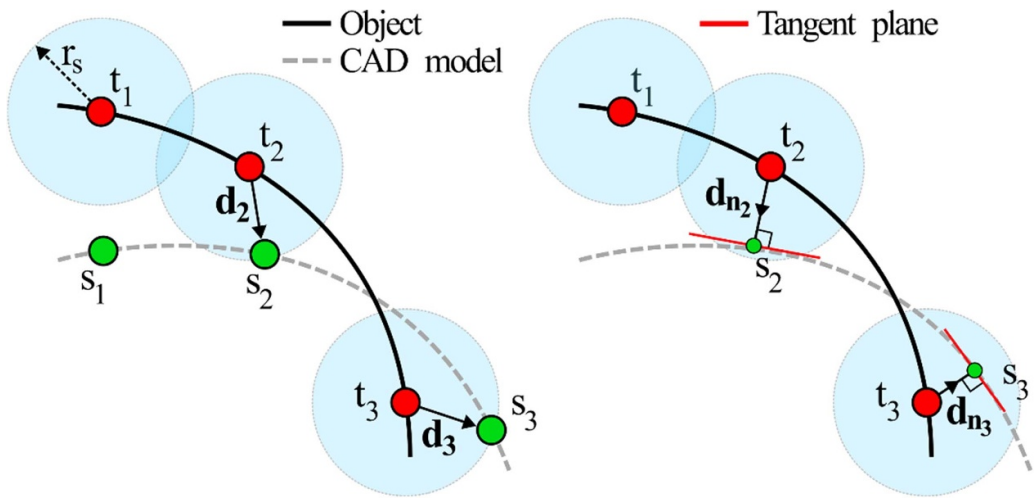

Figure 2. Schematics of the working principle for point-to-point ICP (left) and point-to-plane ICP (right) for the registration of arbitrarily shaped CAD models to experimental object surface measurements. Registration based on the minimization of an error metric defined between the target points (red, object) and source points (green, CAD model) .

the source points (see equation (2)). Hence the name point-to-plane ICP,

$$\varepsilon(\boldsymbol{M}) = \sum_{(s,t\in K)} \left((\boldsymbol{M}\boldsymbol{s} - \boldsymbol{t}) \cdot \boldsymbol{d_n}\right)^2. \tag{2}$$

Note that different from point-to-point ICP, the point-to-plane ICP requires computation of the source points $\boldsymbol{s}$ at each iteration. Source points are therefore not fixed with respect to the CAD model. They rather float on its surface, depending upon the presence of target points within the search radius. Unless the distribution of the source points is known, the point-to-plane ICP is adopted in the present work.

3. Experimental setup and measurement procedures

3.1. Test objects

Different test objects with increasing geometrical complexity are used in the present study: a cube of 12 cm side-length, a truncated wing of 18 cm chord length (and 10.8 cm span) and a 1:8 scaled cyclist of 22 cm length (wheeltip to wheeltip).

The cube and wing are 3D printed using fused deposition modeling and the cyclist with stereolithography. The nominal manufacturing accuracy of the cube, wing and cyclist are approximately 0.3 mm, 0.1 mm and 0.1 mm respectively. Two versions of each object are produced; one includes retro-reflective markers of 1.2 mm $\pm$ 0.1 mm diameter, positioned at known locations along the surface, which enable the use of the point-to-point ICP registration technique (section 4.1). The other is marker free (plain mat black) and are used to investigate active optical marking as discussed in section 3.3. The manufactured objects are shown in figure 3.

3.2. Imaging system

The imaging system comprises seven CMOS cameras (1Mpx, 5400 fps) positioned as to extend the tomographic aperture around any object placed within the measurement volume, without optimizing optical access for one object specifically (see figure 7). Two directions of illumination are provided by two LaVision *flashlight-300* LED's operated at a 33 μs pulse duration. The total measurement volume is approximately 40 $\times$ 40 $\times$ 30 cm^3, which includes the whole model and some of the ground plate around it. A summary of the parameters for the imaging setup and particle tracking are provided in tables 1 and 2.

3.3. Object marking and measurements

Three surface marking techniques are employed: (1) markers are incorporated at prescribed locations during the manufacturing process; (2) the object is illuminated at a single point with a beam laser pointer; (3) the laser beam is split into a multitude of directions resulting in simultaneous multi-point optical marking (approximately 10–20 points on the object surface).

The first technique requires object illumination, which is provided by the LED system (figure 4(a)). As such, the images require pre-processing to eliminate the light reflected from the model surface, by means of sliding minimum subtraction and intensity normalization. Despite a single image being sufficient for the triangulation of the surface markers in theory, a set of 100 recordings is collected to reduce the background noise (sequence minimum intensity subtraction). Any residual low intensity background is removed by subtracting a constant, low-value intensity. An example of a pre-processed image of the cyclist including incorporated markers and illuminated with LED is shown in figure 4(b). The resulting images return easily detectable surface markers with the iterative particle

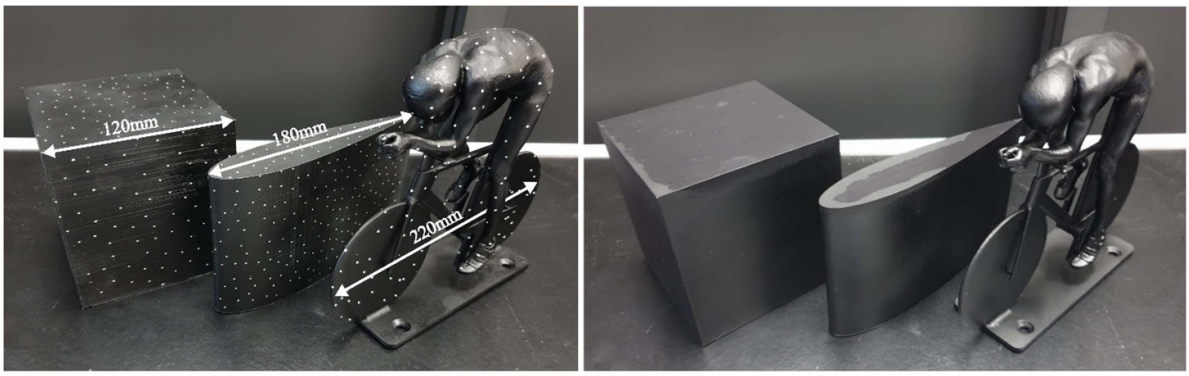

Figure 3. Manufactured cube, truncated wing and scaled cyclist test objects. Version including incorporated retro-reflective markers on the left and version left plain mat black on the right.

Table 1. Imaging system and parameters.

Camera		C1	C2	C3	C4	C5	C6	C7
Resolution	[px]	1024 × 1024						
Pixel pitch	[μm]	20						
Focal length	[mm]	60	50	60	50	60	50	60
F-number		32	22	22	16	22	22	32
Magnification		0.05						
Angular camera offset	[°]	45						

reconstruction algorithm (IPR, Wieneke 2013), available in the LaVision *DaVis 11* software.

While illuminating the objects with the laser pointer, LED illumination is not needed, which leads to images with minimal background intensity from ambient light. Images of the objects are acquired at a frequency of 25 Hz while manually sweeping the laser pattern across the object surface, which is sufficiently covered in under a minute (approximately 1000 images are recorded). A single image of the cube, illuminated with the multi-point laser is shown in figure 4(c) and the pre-processed result in figure 4(d). In this case, the 3D positions of the marked points are triangulated, using IPR, at each frame separately and later combined to provide a dense cloud of target points. Examples of the target point clouds obtained using three different object marking techniques on the cyclist are shown in figure 5. Incorporated markers appear with the lowest surface concentration as they are constantly present during the experiment and interfere with the process of flow tracer detection when their images overlap. Laser marking is performed prior to the experiment and an arbitrarily large number of points can be accumulated. The multi-point marking technique allows increasing further the number of marked points, as shown in figure 5(c). Since the markers within the images are rarely in view by all cameras simultaneously, no marker specific optical transfer function (Schanz *et al* 2013) could be created and used for marker triangulation. Point clouds such as those shown in figure 5 are used without further processing for object registration of which the results are discussed in section 4.

3.3.1. Optical coverage of the marked objects. Not all sides of the object can be viewed from all directions. For the same principle, also the markers cannot be viewed simultaneously by all cameras. Following the discussion in Hysa *et al* (2023), the detection rule that a marker is recognized only if present in all views will be referred to as monolithic, in that the imaging system operates in the whole measurement domain as a single entity. In this case the marker detection process is hindered at several parts of the object surface, leading to measurement volume erosion. Figure 6(a), illustrates the condition where all seven cameras are used in a *monolithic* configuration to triangulate the markers produced by projecting a multi-point laser onto the cube's surface. Only the top face of the cube is in view to all cameras simultaneously. As a result, only those markers are detected, while those on the sides cannot be measured as they are partly obscured to some cameras. Paradoxically, increasing the number of cameras in a monolithic imaging system further erodes the measurement volume. To overcome this problem in a multi-camera setup, the imaging system can be *partitioned* into a number of independent groups (Hysa *et al* 2023). In figure 6(b), groups of three cameras are considered to detect the same markers. An increase in the surface area onto which markers can be triangulated is apparent, strongly benefiting the object registration. Partitioning further into more groups of only two cameras maximizes the amount of object surface where markers can be detected, as shown in figure 6(c). An inverse relationship exists, however, between the number of cameras involved in 3D triangulation and the formation of false triangulations (ghost particles, Elsinga *et al* 2011), which complicates the process of object registration.

Considering the above, marking the object using only a single point at a time (e.g. from a laser pointer), eliminates the problem of ghost particle formation even when only two cameras are used for the triangulation. This is illustrated in figure 6(d). To avoid excessive ghost particle formation while maximizing surface coverage, both incorporated markers and multi-point laser markers on the different objects are triangulated using a partitioned setup with a group size of three cameras. For the triangulation of the single-point laser markers, group sizes of two are used instead.

Note that the problem of measurement volume erosion in a monolithic setup also holds for the 3D triangulation of flow

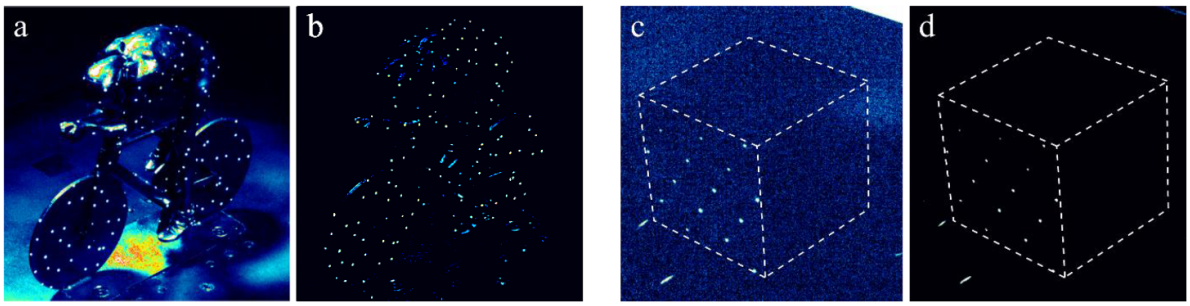

Figure 4. Raw (a) and pre-processed (b) image of the cyclist object with incorporated markers illuminated with LED light. Raw (c) and pre-processed (d) images of the cube (in dark environment) marked with multi-point laser.

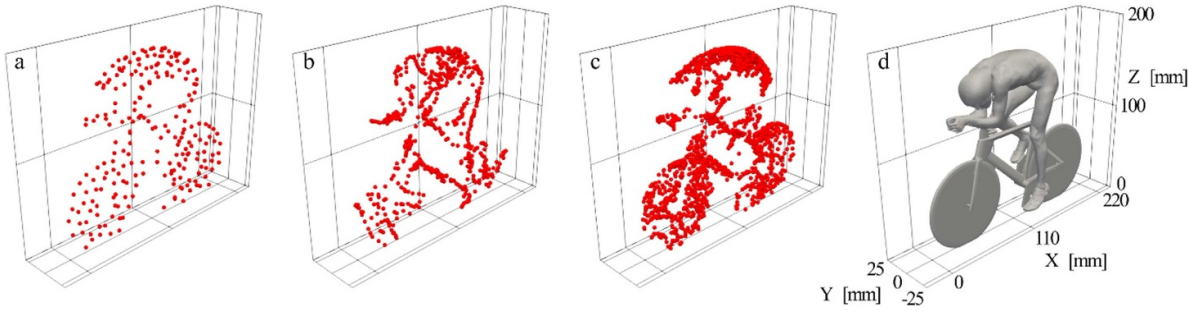

Figure 5. Target point clouds as obtained from different object marking techniques on the cyclist. (a) Incorporated markers. (b) Single-point laser markers. (c) Multi-point laser markers. (d) Cyclist CAD model as reference.

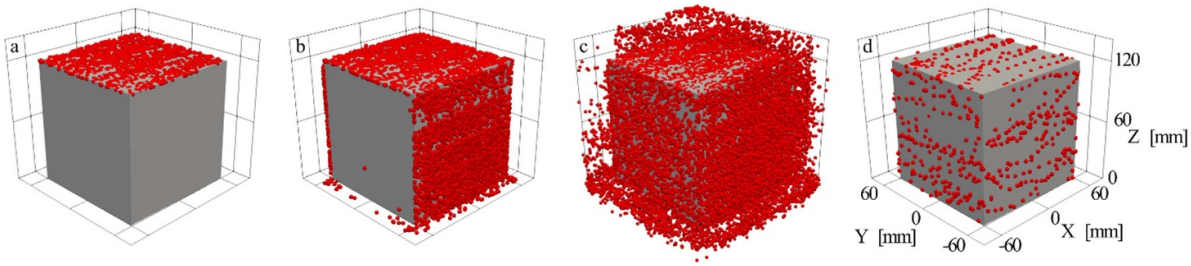

Figure 6. Markers detected on the surface of the cube object as produced from multi-point laser projection. (a) Monolithic approach, (b) partitioned approach with groups of three cameras and (c) two cameras. (d) Detected markers as produced from single point projection with the partitioned approach with groups of two cameras.

tracers around 3D objects as will be discussed in sections 4.3 and 4.4. A partitioned approach with small groups (2–3) of cameras, such as that used in Hysa *et al* (2023) to increase the volume coverage comes, however at the cost of a higher occurrence of ghost particles. It may therefore only be viable for the object registration and not for flow marker tracking in which the particle density is typically considerably higher.

3.4. Wind tunnel measurement conditions

Volumetric flow measurements are performed through large-scale particle tracking. The experiments are performed in a low-speed open jet wind-tunnel, featuring a $60 \times 60\,\mathrm{cm}^2$ cross-section, where a flat plate with elliptical leading edge hosts the selected object. The free stream velocity is $8\,\mathrm{m\,s}^{-1}$ or $10\,\mathrm{m\,s}^{-1}$, depending on the object, with approximately 1% turbulence intensity. A schematic is provided in figure 7.

The flow is seeded with HFSB (Bosbach *et al* 2009) by a $0.5\,\mathrm{m} \times 1\,\mathrm{m}$ seeding rake containing 200 bubble generators upstream of the wind-tunnel contraction. The mean diameter of the neutrally buoyant bubbles is 350μm and at a production rate of 6×10^6 bubbles s^{-1} (Saiz *et al* 2022) a seeding concentration of 1.2 bubbles per cubic centimeter (b cm^{-3}) is achieved at $10\,\mathrm{m\,s}^{-1}$ freestream velocity. The seeding density in the images is approximately 0.02 particles per pixel (ppp). The pre-processed images are used as input for the STB particle tracking algorithm available in DaVis 11. The measurement conditions are summarised in table 2.

Velocity measurements are performed around each of the objects by tracking the HFSB inserted in the flow in the wind tunnel settling chamber. The freestream velocity for the cyclist case is $8\,\mathrm{m\,s}^{-1}$ and for the cube and wing it is $10\,\mathrm{m\,s}^{-1}$. This yields Reynolds numbers of 60 000, 80 000 and 120 000 respectively (cyclist torso length = 90 mm is used as reference length). Images are recorded at a rate of 3kHz. For each

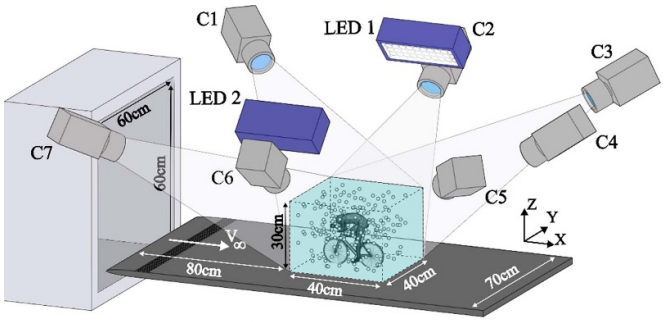

Figure 7. Experimental setup for both velocity field and object registration measurements: seven camera imaging system, LED-illumination, HFSB flow tracers and a plate for model mounting positioned downstream of an open-jet wind-tunnel.

Table 2. Wind tunnel experiment parameters.

Freestream velocity	($m\,s^{-1}$)	8 (cyclist) 10 (wing, cube)
Measurement volume	[cm^3]	$40 \times 40 \times 30$
Seeding concentration	b cm^{-3}	1.2
Acquisition frequency	[Hz]	3000
Images per run		5000
Particle image density	[ppp]	0.02

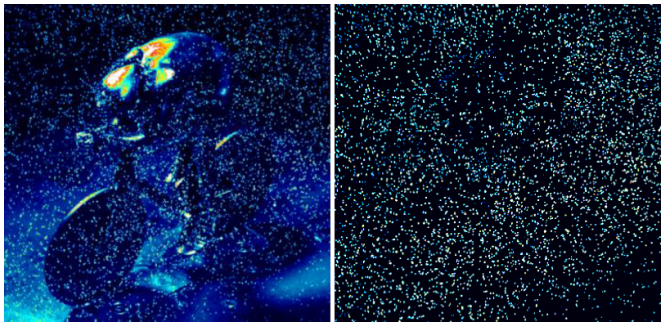

Figure 8. Raw (left) and pre-processed (right) recording of the plain black scaled cyclist object immersed in HFSB seeded flow.

object, a measurement consists of 5000 images for a duration of 1.67 s. The same conditions are repeated with the objects that incorporate retro-reflective markers. A raw instantaneous image of the cyclist model immersed in the flow is shown in figure 8-left.

For a reliable particle detection, background reflections need to be removed. The image pre-processing operations involve minimum pixel intensity subtraction and image intensity normalization. Finally, a small constant value ($2\% - 3\%$ of particle peak intensity) is subtracted to eliminate residual low intensity noise in the background. The effectiveness of the pre-processing steps is shown in figure 8-right.

4. Results

4.1. Point-to-point registration

In this section, reference registrations are performed for comparison with later registrations in section 4.2. Such reference registrations are performed making use of the objects that include incorporated markers at known positions along the surface. Therefore, the point-to-point correspondence is imposed, which is considered the most accurate and robust option. Yet, imperfection in marker triangulation and in the manufacturing of the test objects result in a finite residual after the reference registration.

The incorporated markers physically present on the objects are detected and triangulated following the procedure described in section 3.3, resulting in a set of target points $\boldsymbol{t}$ for each object. The corresponding CAD model is virtually marked providing the source points $\boldsymbol{s}$. In this scenario a direct correspondence exists between the target and source points and point-to-point ICP can be applied. The result of the registration is shown in figure 9, where the red dots indicate the triangulated position of the incorporated markers on the object surface (target, $\boldsymbol{t}$). The green markers, instead, are the source points $\boldsymbol{s}$ associated to the CAD representation of the model. As it can be observed in figure 9 a subset of the source points is matched to the triangulated target points. Reasons for unmatched source points are twofold: first, some target points are simply not triangulated as they are not in view by the set minimum number of three cameras (see section 3.4). Second, correspondences between source and target points in the ICP registration procedure are established based on the defined search radius as mentioned in section 2. Target points without a corresponding source point within the search radius ($r_s = 1.5$ mm is used) are not visualized as they are ignored during the registration procedure. Statistics in terms of distance from target to source points are provided in the histograms of figure 10 below.

Out of all markers physically present on the individual objects, 66%, 92% and 46% have been triangulated and correctly matched to their corresponding point on the CAD model within 1.5 mm ($= r_s$) for the cube, wing and cyclist respectively. The average discrepancy (distance between the triangulated target point and the corresponding source point position) is 0.8 mm. Such discrepancy is associated with the 3D triangulation uncertainty as well as that of model manufacturing. It is observed that triangulation of the incorporated markers are consistently offset from the true marker location by a distance on the order of the marker radius. Furthermore, large markers, in combination with the direction of illumination are an additional source of uncertainty in the determination of the marker centers.

4.2. Point-to-plane based object registrations

The reference registrations are used as a baseline to assess the registrations based on the different marking techniques.

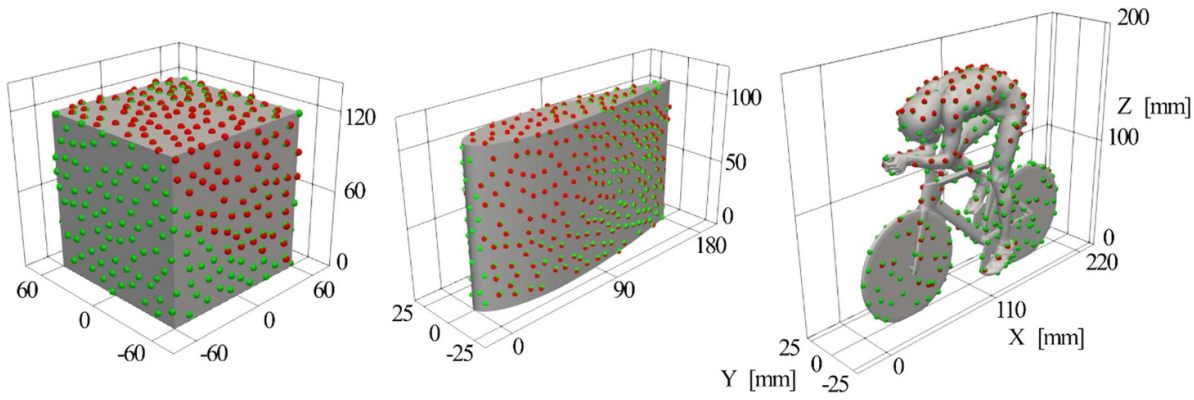

Figure 9. Reference (point-to-point) registrations for the three objects. Green dots represent the distribution of the incorporated markers on the object surface (source **s**). Red dots represent the experimentally triangulated and registered markers (target **t**) .

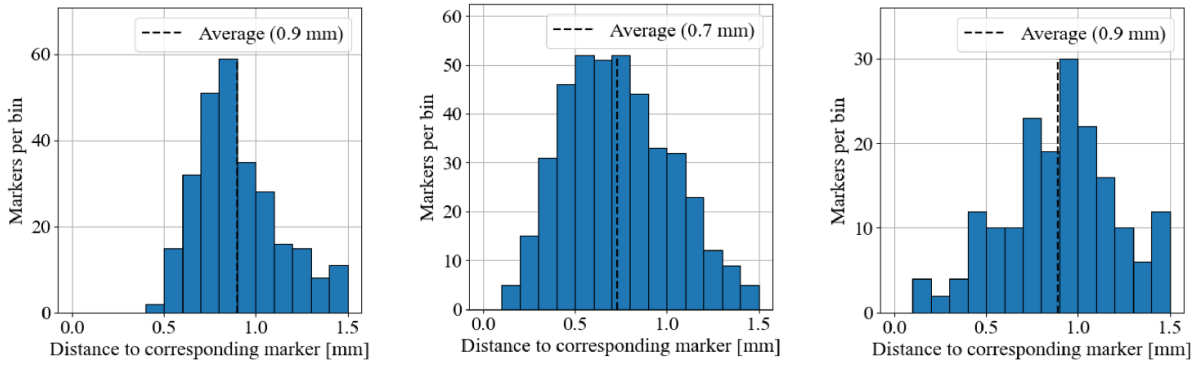

Figure 10. Histograms of point-to-point corresponding marker distances (source to target) after reference object registrations. Left to right for the cube, truncated wing and scaled cyclist respectively.

A comparative analysis is made of three methods: incorporated markers (without making use of their known distribution as done for the reference registration), projection of a single laser point, or multitude of points along the object surface. Furthermore, these techniques are applied to three objects, resulting in nine conditions for the object registration. Figure 11 illustrates three registration examples each on a different object, where target points are color-coded with the signed distance to the registered CAD model surface. Positive and negative values correspond to markers outside and inside of the objects respectively. These object registrations make use of point-to-plane ICP. The object registrations are performed using a final search radius of 1.5 mm; hence, only those markers within a distance to CAD model surface below 1.5 mm are included in the figures.

For the incorporated markers on the cube, a partitioned system, where cameras are arranged in triplets is used (see section 3.3.1). Since the front face of the cube is in view by only two cameras, markers on the frontal face are not reconstructed. On the side face of the cube, the discrepancy varies within $0.5 - 1.0$ mm, with a pattern indicating a non-flat cube face. The top face yields consistently smaller errors. Yet, the gradient in the color-coded points indicates a slightly slanted top face of the cube. The truncated wing and cyclist yield lower values of the discrepancy with no specific spatial pattern, indicating a smaller effect of manufacturing artefacts in these cases. The mean absolute values of markers discrepancy, denoted $\delta_{s,t}$ (discrepancy between source $\boldsymbol{s}$ and target $\boldsymbol{t}$), are reported in table 3.

The cube registration yields a $\delta_{s,t}$ of about 0.5 mm, with only minor differences among the marking techniques. For the truncated wing and scaled cyclist, $\delta_{s,t}$ is around 0.3 mm and variations among marking techniques below 0.1 mm. The registration performed using the single-point laser marking yields the largest values of $\delta_{s,t}$. This is not ascribed to the limited number of points, but rather a side effect of the increased surface coverage achieved using the partitioned approach with camera pairs instead of triplets (see section 3.3.1). The increased coverage imposes a stricter constraint to the model registration as the point-to-plane algorithm allows some relative sliding. Increased model surface coverage with a given marking technique is expected to benefit the determination of the model position through registration; however, this is not necessarily represented in the average absolute distance from markers to the CAD model $\delta_{s,t}$. Therefore, the dice similarity coefficient (DSC, Dice 1945) with respect to the reference registration is tabulated in table 4. The similarity coefficient is computed as the overlapping volume between a registered CAD model and corresponding reference registration, divided by the total volume of a model. The coefficient varies from 0 (no overlap) to 1 (perfect overlap) (Saiti and Theoharis 2020).

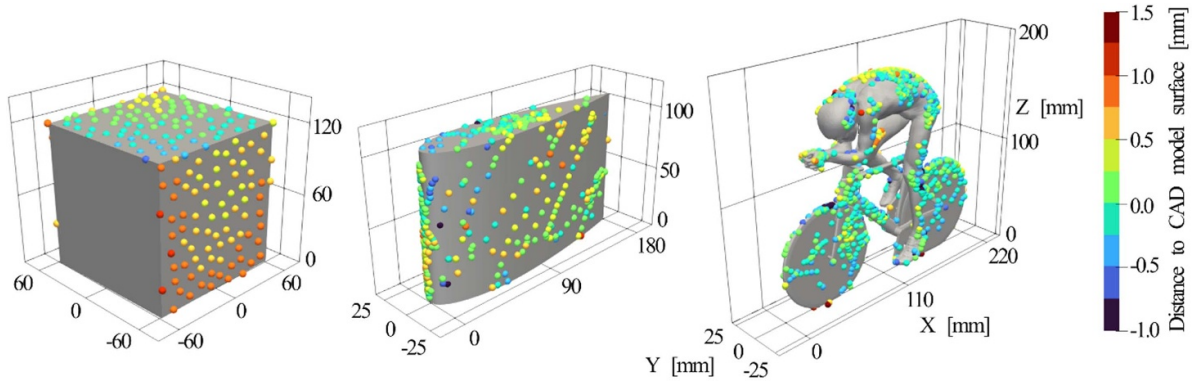

Figure 11. Example object registrations of the cube with respect to triangulated incorporated markers (left), truncated wing to single-point laser markers (middle) and scaled cyclist to multi-point laser markers (right) .

Table 3. Object registration results in mean absolute distance from markers to registered CAD model ($\delta_{s,t}$) .

$\delta_{s,\,t}$ (mm)	Cube	Wing	Cyclist
Incorporated markers	0.473	0.274	0.278
Multi-point laser	0.482	0.186	0.258
Single-point laser	0.513	0.275	0.352

Table 4. Object registration results as similarity coefficient to the corresponding reference registration.

DSC (−)	Cube	Wing	Cyclist
Incorporated markers	0.989	0.992	0.971
Multi-point laser	0.989	0.992	0.949
Single-point laser	0.991	0.989	0.949

All registrations return a high value (approximately 0.95–0.99) for the similarity coefficients indicating a correct positioning of the CAD model in the measurement space. While the increased surface coverage on the cube using the single-point laser marking seemingly produces higher local values of marker disparity, the similarity coefficient indicates an overall marginally improved matching. For the wing instead, most of the surface area is covered by the camera triplets (see section 4.3). No significant increase in the surface coverage is therefore achieved when moving to camera system partioning in groups of two in combination with single-point marking, resulting in a slightly decreased similarity coefficient with respect to the other marking techniques. Both the multi- and single-point laser marking score lowest in terms of similarity coefficient for the cyclist registration. This is ascribed to an uneven distribution of the manual laser marking biased towards higher density at the positive y-side of the cyclist, shifting the registrations with respect to the reference.

4.3. Modeling of optical occlusion

The object registrations provide a CAD representation of the models used during the experiment, positioned and oriented within the experimental measurement volume/coordinate system. Since the camera locations and orientations are determined within this coordinate system as well, the optical access of the imaging setup can be determined throughout the measurement volume through the use of ray-casting (Möller and Trumbore 1997). The number of cameras having optical access to a certain region within the measurement volume is referred to as the camera coverage rank R_C. The R_C over the model surface and two planes within the measurement volume are visualized in figure 12 for the three objects. The value of R_C on the registered model surfaces provides insight into the observed differences when using incorporated markers or the single-point laser marking from section 4.2. Especially on the cube, $R_C = 2$ on one of the side faces and the coverage is increased significantly when groups of two cameras are used for a partitioned setup.

The variation in the R_C over the planes visualized in figure 12 follows the expected behavior of the seven camera imaging system as shown in figure 7: out of the three objects, the wing is smallest in height hence there is an R_C of 7 towards the edges of the plane at the object base. For all objects, the R_C in the shown planes varies across shapes resembling projected shadows from the perspectives of the individual cameras. For the cube, the majority of the planes feature $R_C \geq 3$ with only a small region in front of the frontal face at $R_C = 2$. For the wing and cyclist, the entirety of the shown planes is in view by at least 3 cameras. The distribution of the R_C throughout the measurement volume is an important factor during the 3D triangulation of flow tracers in particle tracking velocimetry measurements. The volume fraction of the total measurement volume in view by a certain number of cameras is shown in figure 13.

The minimum value considered for camera rank is two as it corresponds to the theoretical minimum for 3D determination of a particle position by triangulation. The total volume of the measurement domain (100%) is calculated assuming a cuboid domain of dimensions 0.4 m $\times$ 0.4 m $\times$ 0.3 m, thus 0.048 m^3, centered around the object (as in figure 7). The volume occupied by the object itself is excluded from the calculation. The volumetric coverage decreases by increasing the camera rank, which justifies the frequent adoption of camera

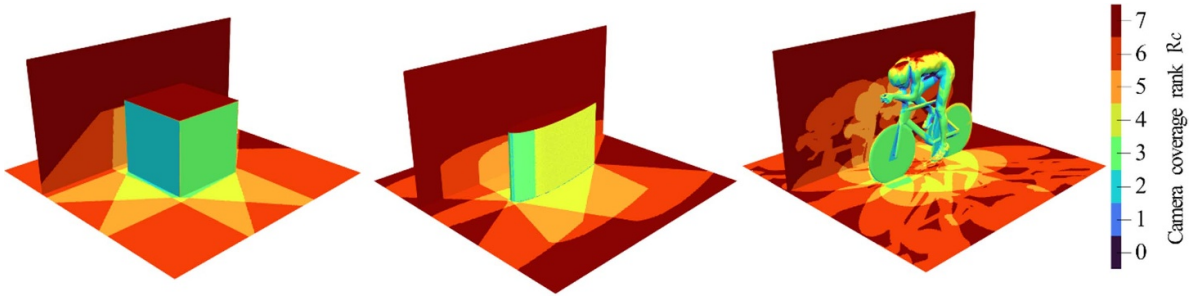

Figure 12. Camera coverage rank (R_C) of the seven camera imaging setup visualized in an x,y-plane at $z = 0$ mm and an x,z-plane at $y = 80$ mm.

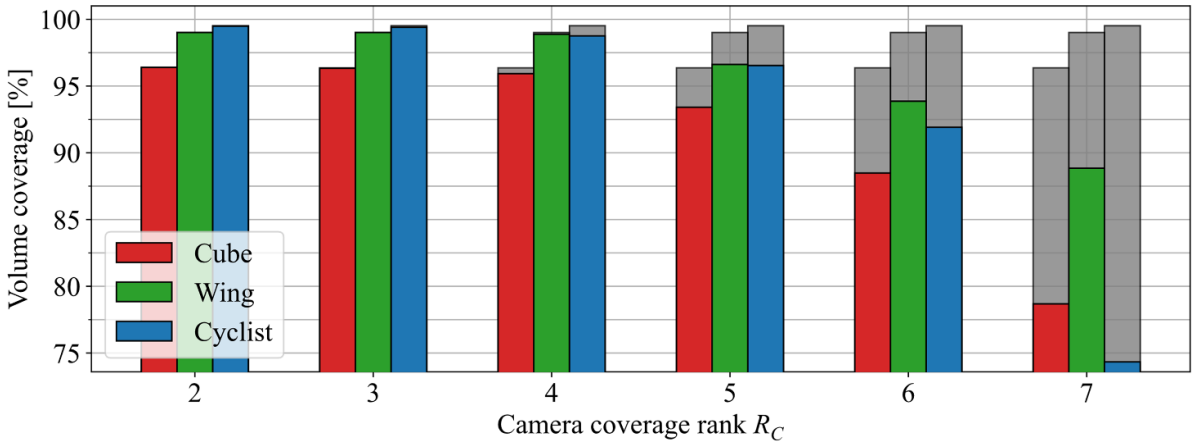

Figure 13. Measurement volume, effective measurement volume (measurement volume—object volume) and effective measurement volume in view by a certain number of cameras simultaneously (camera coverage rank R_C) for the cube, truncated wing and scaled cyclist object.

system partitioning in 3D experiments. Increasing R_C up to a value of 4 yields minor variations of the volumetric coverage. This behavior also depends upon the placement of the cameras (as discussed in Hysa *et al* 2023) and the shape and orientation of the obstructing object. For instance, the wing, with its smallest height and relatively small thickness, results in the smallest decrease in volume coverage when increasing R_C. Further increasing R_C beyond 5 results in a rapid reduction of volumetric coverage, with the monolithic system yielding a volumetric coverage of below 80% for the cube and cyclist.

The above discussion becomes of vital importance during particle tracking, in the context of the information provided in section 3.4. Without registration of the object in the experimental measurement domain and determination of the variation of the camera coverage rank throughout said domain, a monolithic imaging system is limited in particle triangulations to only the intersected volume of all camera field of views, hence in this experiment the volume coverage at $R_C = 7$. Additionally, the 'eroded' measurement volume in such a monolithic setup is mostly confined to regions in close proximity of the object surfaces which are especially relevant in the understanding of near wake/surface flow properties. Overcoming such measurement volume erosion can be achieved through partitioning of the imaging setup into independent camera groups as done in section 3.3.1. In a partitioned approach, the measurement volume instead is the union of all regions measured by the camera groups. The downside of the partitioned approach being that a limited number of cameras is used for the triangulation of flow tracers, becoming critical at higher imaging density of seeding particles as typically done in tomographic or particle tracking experiments. The latter circumstance causes the frequent occurrence of ghost particles (Elsinga *et al* 2011).

To combine the benefits while mitigating the disadvantages of the monolithic and partitioned approaches, the now known object position information can be incorporated within the particle tracking approach which is referred to as (OA) monolithic 3D particle imaging. Following the OA-monolithic method, the specific lines-of-sight obstructed by the object are not considered for each camera and particle triangulation is performed using the optimum (maximum) number of cameras all throughout the domain. This method therefore renders partitioning obsolete and greatly reduces the problem of ghost particles formation. OA particle tracking, as it has been implemented into the DaVis 11 software, has been discussed by Wieneke and Rockstroh (2024) and will be used throughout the remainder of this manuscript.

4.4. Volumetric detection of flow tracers

The volumetric distribution of the camera coverage rank after object registration, such as shown in figure 12, is used to

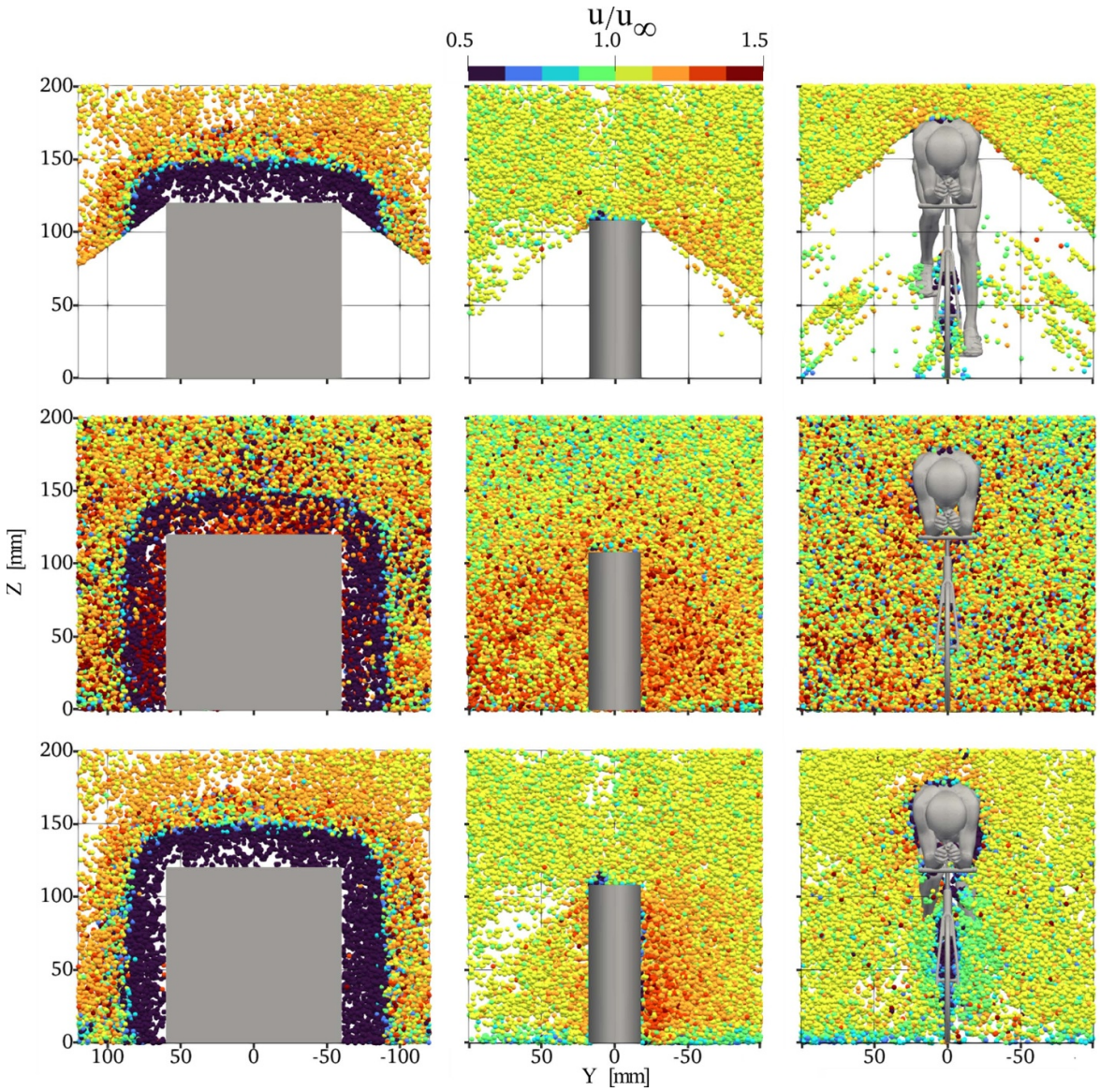

Figure 14. Particle triangulations in a 50 mm deep $Y-Z$ plane centered at the midpoint of the object. Top row: triangulations using monolithic approach (M_7-IPR). Middle row: triangulations using a partitioned approach (groups of 3, P_3-IPR). Bottom row triangulations using object aware monolithic approach (OA_7-IPR). Particles colored by streamwise velocity component.

perform OA-particle triangulation/tracking by a monolithic approach. In particular, the IPR (Wieneke 2013) method is used. Three methods of reconstruction are then compared, for the given set of seven cameras: the monolithic approach (M_7-IPR), the partitioned approach with camera triplets (P_3-IPR) and the object aware monolithic method (OA_7-IPR). In figure 14, particle triangulations over 200 measurement snapshots are shown in a 50 mm thick volume set across the freestream directions centered around the midpoint of the object.

The top row shows the particles reconstructed using M_7-IPR, where the measurement suffers from significant regions void of particles. These examples illustrate the entity of measurement volume erosion associated to the monolithic approach, as the loss of optical access from each single camera produces a void. In the second row, the reconstruction from P_3-IPR is shown. Clearly, the volumetric coverage is restored, with no clear presence of void regions. The individual particles are color-coded by velocity magnitude. The flow in the region well above the object is expected to exhibit a rather stationary behaviour as it pertains to a potential flow. Instead, in the second row, the scattered occurrence of data with strong variations of the velocity magnitude is associated to erroneous measurements due to ghost particles. Their occurrence is particularly pronounced for P_3-IPR, compared to the monolithic method. The small number of cameras in each sub-group is responsible for this condition (Elsinga *et al* 2011).

Furthermore a partitioned setup produces multiple detections of the same tracers in regions where the measurement regions from different camera triplets overlap and data post-processing is required to avoid biasing effects. Ghost particles formed from different camera groups instead, do not coincide and they accumulate in the measurement domain. The analysis performed with OA_7-IPR is shown on the bottom row.

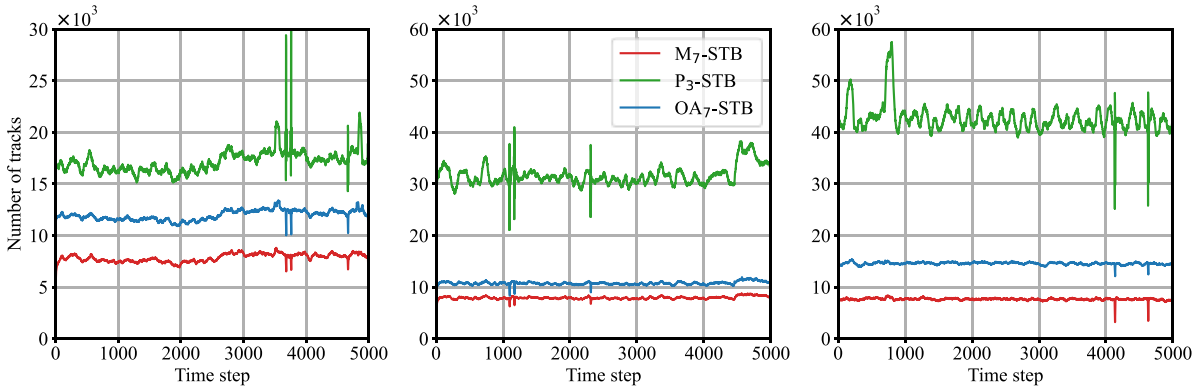

Figure 15. Number of simultaneously tracked particles using a monolithic (M_7-STB), partitioned (P_3-STB) or OA-monolithic approach (OA_7-STB). Left: cube; middle: truncated wing; right: scaled cyclist.

The results clearly indicate that both problems of measurement volume erosion and excessive ghost particle formation are mitigated. Particle detection can be performed throughout the measurement volume when in view by at least three cameras, yielding the same volume coverage as the partitioned setup, whilst using more cameras for the triangulation if possible. Not only does this reduce the formation of ghost particles with respect to the partitioned setup but even compared to the monolithic approach. This is especially visible around the cyclist model where in the top figure still a considerable number of unphysical data points are found for M_7-IPR regardless of the involvement of all seven cameras in the triangulation. The reason for this is the large number of particles in the camera images originating from regions in the measurement volume at a R_C of less than seven. Such particles are not triangulated and therefore not eliminated from the particle images leaving them able to contribute to the formation of ghost particles (Wieneke 2013, Schanz *et al* 2016).

4.5. Particle tracking

The ultimate purpose of the experiment is that of obtaining the accurate velocity field distribution around the object of interest. The motion of the detected flow tracers is determined by tracking them throughout the measurement volume. The STB algorithm (Schanz *et al* 2016) efficiently performs this task. The number of simultaneously detected tracks over time provides insight into the behaviour of object aware particle tracking (OA_7-STB) compared to the monolithic (M_7-STB) and partitioned STB approach (P_3-STB), this is plotted below in figure 15. Tracks are accepted when a tracer is detected along at least four consecutive timesteps.

The monolithic approach yields the smallest number of tracks as a result of the low volumetric coverage. Providing object information restores the measurement volume, with a relative increase in the number of tracks that varies from 40% to 90% depending on the object. The partitioned system produces the largest number of tracks, varying from 2 to 4 times more than the monolithic method. As discussed for the case of the triangulation analysis, such a large number of tracks is ascribed to the frequent occurrence of ghost particles, which needs to be scrutinized looking at their time coherence. A parameter to consider when assessing the reliability of tracked particles is the tracking ratio, defined as the number of tracked particles (figure 15), divided by the number of triangulated particles. The values of the average tracking ratio are tabulated in table 5.

Table 5. Average ratio of tracked over triangulated particles (tracking ratio) for the three tracking approaches and objects.

Tracking ratio	Cube	Wing	Cyclist
M_7-STB	0.92	0.87	0.78
P_3-STB	0.2	0.28	0.3
OA_7-STB	0.77	0.74	0.76

Table 6. Average track length for the three tracking approaches and objects.

Average track length (time steps)	Cube	Wing	Cyclist
M_7-STB	75	54	13
P_3-STB	37	14	17
OA_7-STB	75	50	71

Since ghost particles do not necessarily follow flow trajectories over time, a large number of ghost particles versus true particles results in a low tracking ratio. For the partitioned approach, three to four times lower tracking ratios are observed compared to the monolithic and object aware approaches. This not only indicates a large number of initial ghost particles as was already shown in figure 14, but also results in significantly increased computation times. The monolithic approach makes use of seven cameras for all triangulations and fewer ghost particles are formed with a high tracking ratio as a result. The object aware (OA) approach additionally triangulates particles in the regions left void in the monolithic method with as few as three cameras. In such regions, a comparatively larger number of ghost particles occurs, lowering the tracking ratio.

Another parameter of interest is the extent for which a single particle can be tracked throughout time, which is shown in table 6, in terms of average track lengths in timesteps. It should be noted that even though particle triangulations using

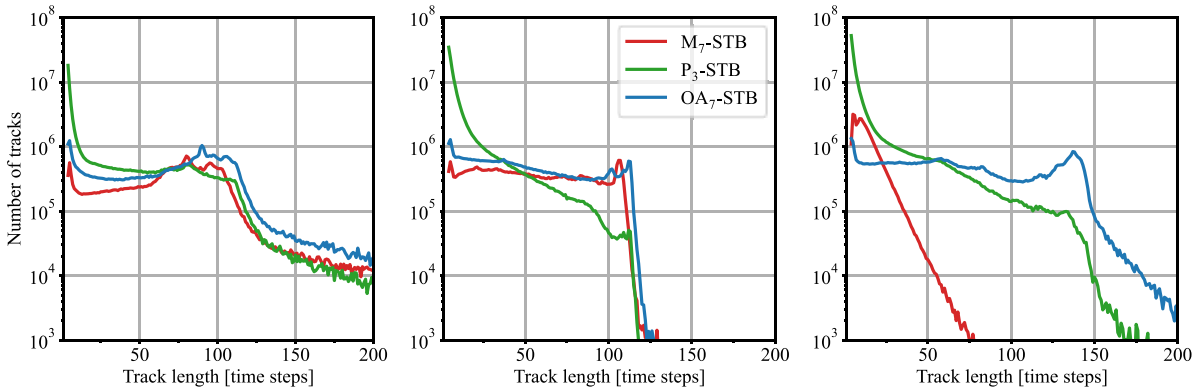

Figure 16. Track length histogram for three particle tracking approaches. Left: cube; middle: wing; right: cyclist.

a simple monolithic approach are limited to regions in view by all seven cameras, once a track has been established, the advancement of the particle only requires that a minimum of three cameras view the particle. This is a specific feature of the STB algorithm, as discussed in Wieneke and Rockstroh (2024) and for other algorithms different logics may be applied to particle detection and tracking. Regions in view by all cameras are typically located away from the objects towards the edges of the measurement volume. Since in these regions particles can be triangulated using the monolithic approach without 'object awareness', particle tracks tend to be initialized far upstream and persist through partially occluded regions resulting in relatively long particle tracks as seen in table 6. The cyclist appears to be an exception to this where many intermittent tracks are observed when crossing interfaces of varying camera coverage R_C resulting in instead much shorter tracks on average. Ghost particles which are assigned to a track typically cannot maintain such a track for extended time resulting in many short tracks instead. This clearly causes a reduced averaged track length for the partitioned setup. The OA approach can both initialize and track particles all throughout the measurement volume producing similar average track lengths to the non- OA approach.

Figure 16 reports the diagrams of the number of particle tracks versus their length (time steps). The results pertain to the full sequence of 5000 timesteps. The combined effect on track length and total number of tracks for the different approaches is a clear indicator of method performance and reliability.

The y-axis is shown on a logarithmic scale, given the order of magnitude difference between the occurrence of short tracks ($\sim$10 timesteps) for the partitioned system. In line with the expected behavior of ghost particles, the number of tracks for increasing track length initially drops rapidly. A peak at short track length is also present for the monolithic and OA methods, however of much smaller magnitude. The value rapidly decreases towards a plateau that lasts till approximately 100 timesteps and then the value decays. This behavior is expected on the basis of the measurement domain streamwise length, the flow velocity and the chosen sampling frequency. A particle in the freestream at 10 $\mathrm{m\,s^{-1}}$ will remain in the domain (of 40 cm length) for approximately 40 ms. At the measurement rate of 3000 fps tracks in the freestream will therefore not exceed 120 timesteps, which justifies the decay on the right end side of the diagrams.

Table 7. Total number of found particle tracks with length bigger or equal to 25 timesteps.

Total tracks $\geqslant 25$ time steps ($\times 10^6$)	Cube	Wing	Cyclist
M_7-STB	34.1	30.8	3.4
P_3-STB	39.2	25.2	44.0
OA_7-STB	49.0	38.8	59.7

Considering the steep gradient in the partitioned curves until track lengths of roughly 25, tracks with length below 25 seem to contain most of the ghost particles. Filtering out these assumed ghost tracks produces a total number of tracks measured as tabulated below.

Overall, figure 16 and table 7, confirm that the OA approach yields both a larger number of tracked particles which are tracked over longer periods of time with respect to the simple monolithic approach. Additionally, the formation of ghost particles is noticeably reduced with respect to the partitioned approach.

4.6. Velocity field measurement

The impact of the object registration technique and of the OA particle reconstruction/tracking is ultimately evaluated in terms of the measured velocity field. The time average velocity distribution is rendered onto a Cartesian grid following the ensemble averaging procedure as described in Agüera *et al* (2016). For this, a bin size of 10 $\times$ 10 $\times$ 10 $\mathrm{mm^3}$ is used with an overlap percentage of 75%, resulting in a grid spacing of 2.5 mm. Within each bin, the velocity is represented by a 2nd order polynomial regression. Both time averaged flow data and time resolved particle tracks are available in Hendriksen 2024. The streamwise velocity field around the cyclist is inspected along an $x-z$ plane at $y = 0$ mm for the monolithic, partitioned and OA approaches (figure 17). No filtering is applied to remove measurement noise or to exclude ghost particles from

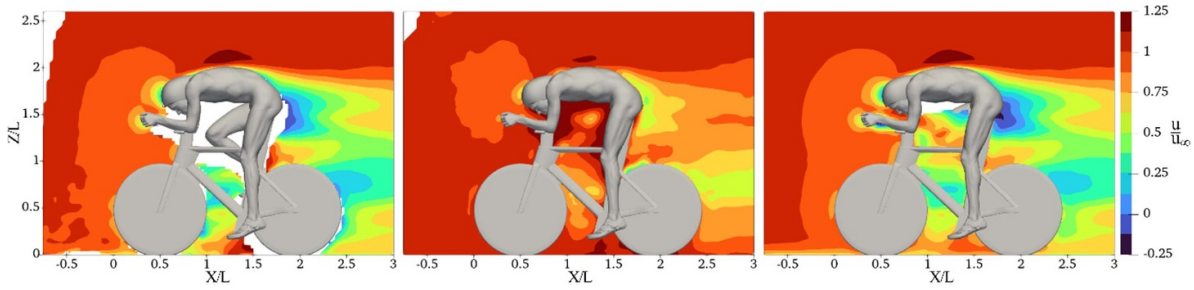

Figure 17. Normalized streamwise velocity field around the cyclist object. Monolithic (M_7-STB), partitioned (P_3-STB) and OA-monolithic (OA_7-STB) particle tracking approach left to right respectively. Freestream velocity of 8 $m\,s^{-1}$. Distances normalized by cyclist torso length $L = 90$ mm.

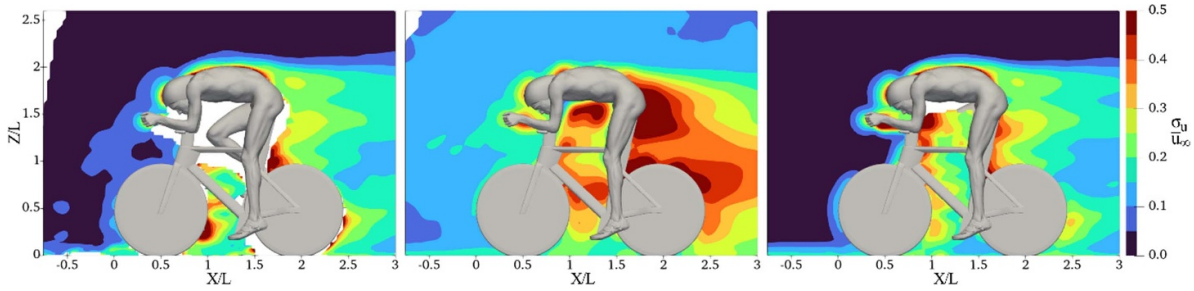

Figure 18. Normalized standard deviation of the streamwise velocity field around the cyclist object. Monolithic (M_7-STB), partitioned (P_3-STB) and OA-monolithic (OA_7-STB) particle tracking approach left to right respectively. Freestream velocity of 8 $m\,s^{-1}$. Distances normalized by cyclist torso length $L = 90$ mm.

the ensemble at each bin. The freestream velocity for the cyclist was set to 8 $m\,s^{-1}$.

The velocity field obtained with the monolithic approach features smaller regions void of data compared to what was shown in figure 14. This is due to the different number of cameras required to triangulate/reconstruct a particle's 3D position (the totality) and to track it using the STB algorithm (only three cameras). The velocity field exhibits a rather uniform value above and upstream of the cyclist, whereas the momentum deficit in the wake is evident, where small regions of reverse flow indicate some local separation at the rear of the athlete. These results are in good agreement with those reported by Jux *et al* (2018) who used robotic volumetric PIV around a full-scale cyclist in the same posture, at the racing speed of 14 $m\,s^{-1}$. Even though the velocity field obtained using the partitioned camera setup does not contain any gaps, it is clearly affected by an excessive number of ghost particles. Ghost particles persisting into the tracks typically originate from the coherent motion of bubbles in the freestream and therefore have unphysically high velocities with respect to their neighbouring tracks. This produces a bias error towards larger velocities which tends to decrease the observed velocity gradients (Elsinga *et al* 2011). This is clearly visible in the middle figure where there is a complete lack of reversed flow throughout the shown plane and relatively large velocity values in regions of expected stagnation such as the helmet and hands.

The velocity field obtained using the OA approach largely resembles that of the monolithic system, except for a reduction in the size of the regions void of data below and behind the cyclist torso. Furthermore, for the monolithic approach, regions in view by less than all seven cameras rely on convection of upstream tracks to provide data. This reduces the overall number of tracks used in the ensemble averaging procedure compared to the OA approach, leading to more jagged velocity contours especially visible upstream of the cyclist and close to the floor.

The random noise caused by ghost particles is examined more closely using the spatial distribution of streamwise velocity fluctuations (standard deviation σ_u) as shown in figure 18.

The flow regions upstream of the cyclist are expected to exhibit a low level of fluctuations, according to the rated turbulence intensity of the wind tunnel freestream; 0.6% (Lima Pereira *et al* 2022). The monolithic approach returns fluctuation levels of approximately 3% and 1.5% when the OA method is applied. The results from the partitioned setup are considerably corrupted, yielding a standard deviation of up to 12% upstream of the cyclist. A similar pattern is observed in the turbulent wake, where the partitioned method yields fluctuations exceeding 50% of the free-stream value and overall twice as high than those measured with the monolithic approach. It may be concluded that the fluctuating velocity field can only be qualitatively addressed by the partitioned approach, in the present case, where the fluctuations appear to be dominated by the contribution of ghost particles. Especially visible in the OA approach is an increase in the standard deviation towards regions of flow stagnation. This can be ascribed to unresolved velocity gradients within the relatively large bins

used for the ensemble averaging and variations in the bubble response time under acceleration (Faleiros *et al* 2019).

5. Conclusion

Object registration methods for volumetric flow measurement techniques are surveyed and compared in the framework of Lagrangian particle tracking. Three object marking methods are considered and applied on objects with varying geometrical complexity which include the use of markers incorporated into the object during manufacturing and the projection of a single- or multitude of markers by means of a laser pointer. Using the point-to-plane ICP algorithm, object registration is applied to the objects which are in the order of 10 cm in size and the found discrepancies between registered objects and the triangulated markers are on average in the order of 0.5 mm. The incorporated markers at known locations are additionally used to perform point-to-point ICP registrations which serve as a reference. The point-to-plane registration accuracy based on the metrics of the similarity coefficients with respect to a reference yields results ranging from 95% to 99%, which is considered sufficiently accurate for the purpose of applying OA particle reconstruction.

Three different regimes of 3D imaging have been considered: monolithic, partitioned and OA monolithic. These methods were compared in terms of volumetric coverage of the domain and the ratio between correct tracks and those due to ghost particles. Several benefits of OA particle tracking are demonstrated. Firstly, the severe problem of erosion of the measurement volume typical of the monolithic multi-camera imaging system is solved, thanks to the selective utilization of cameras with unobstructed views. The second problem noticed for the partitioned system is the large amount of ghost particles and associated measurement error. Also in this case, the OA monolithic technique maximizes the number of cameras involved in particle triangulation; dramatically reducing the occurrence of ghost particles, benefitting accurate flow field determination. It may be concluded that partitioning a multi-camera 3D imaging system is the last resort for the measurement around an object and this technique may be considered only when a model for the object is not available or it cannot be reliably measured. Using either statically triangulated incorporated or optical markers, the current approach of OA particle tracking is limited to rigid and stationary objects with or without a-priori applied markers. In the future, the extension to moving and flexible objects is in principle supported by the framework of OA particle tracking but will require more sophisticated methods of representing not only the potentially varying position but also shape of the object as a rigid CAD model registration will no longer suffice.

Data availability statement

The data that support the findings of this study are openly available at the following URL/DOI: 10.4121/a2e5b234-cd95-4749-84b2-0f96937ae3cf.

ORCID iDs

L A Hendriksen https://orcid.org/0009-0006-7229-0176
A Sciacchitano https://orcid.org/0000-0003-4627-3787
F Scarano https://orcid.org/0000-0003-2755-6669

References

Acher G, Thomas L, Tremblais B, Gomit G, Chatellier L and David L 2019 Simultaneous measurements of flow velocity using Tomo-PIV and deformation of a flexible wing *13th Int. symp. on particle image velocimetry–ISPIV*
Adhikari D and Longmire E K 2012 Visual hull method for tomographic PIV measurement of flow around moving objects *Exp. Fluids* **53** 943–64
Adhikari D and Longmire E K 2013 Infrared tomographic PIV and 3D motion tracking system applied to aquatic predator-prey interaction *Meas. Sci. Technol.* **24** 1255–260
Agüera N, Cafiero G, Astarita T and Discetti S 2016 Ensemble 3D PTV for high resolution turbulent statistics *Meas. Sci. Technol.* **27** 124011
Besl P and McKay N D 1992 A method for registration of 3-D shapes *IEEE Trans. Pattern Anal. Mach. Intell.* **14** 239–56
Bosbach J, Kühn M and Wagner C 2009 Large scale particle image velocimetry with helium filled soap bubbles *Exp. Fluids* **46** 539–47
Cakir B O, Gonzalez Saiz G, Sciacchitano A and van Oudheusden B 2022 Dense interpolations of LPT data in the presence of generic solid objects *Meas. Sci. Technol.* **33** 124009
Chen Y and Medioni G 1992 Object modelling by registration of multiple range images *Image Vis. Comput.* **10** 145–55
Depardon S, Lasserre J J, Boueilh J C, Brizzi L E and Borée J 2005 Skin friction pattern analysis using near-wall PIV *Exp. Fluids* **39** 805–18
Dice L R 1945 Measures of the amount of ecologic association between species *Ecology* **26** 297–302
Elsinga G E, Scarano F, Wieneke B and Van Oudheusden B W 2006 Tomographic particle image velocimetry *Exp. Fluids* **41** 933–47
Elsinga G E, Westerweel J, Scarano F and Novara M 2011 On the velocity of ghost particles and the bias errors in tomographic-PIV *Exp. Fluids* **50** 825–38
Faleiros D E, Tuinstra M, Sciacchitano A and Scarano F 2019 Generation and control of helium-filled soap bubbles for PIV *Exp. Fluids* **60** 1–17
Grille Guerra A, Scarano F and Sciacchitano A 2024 On the scalability of helium-filled soap bubbles for volumetric PIV *Exp. Fluids* **65** 23
Hendriksen L A, Sciacchitano A and F Scarano 2024 Object registration techniques for 3D particle tracking *4TU* (https://doi.org/10.4121/a2e5b234-cd95-4749-84b2-0f96937ae3cf)
Hysa I, Tuinstra M, Sciacchitano A and Scarano F 2023 A multi-directional redundant 3D-PIV system for ship deck wind interactions *15th Int. Symp. on Particle Image Velocimetry*
Jeon Y Jin and Sung H Jin 2012 Three-dimensional PIV measurement of flow around an arbitrarily moving body *Exp. Fluids* **53** 1057–71
Jux C, Sciacchitano A and Scarano F 2021 Object surface reconstruction from flow tracers *Exp. Fluids* **62** 1–19
Jux C, Sciacchitano A, Schneiders J F G and Scarano F 2018 Robotic volumetric PIV of a full-scale cyclist *Exp. Fluids* **59** 74
Langley K R, Hardester E, Thomson S L and Truscott T T 2014 Three-dimensional flow measurements on flapping wings using synthetic aperture PIV *Exp. Fluids* **55** 1–16
Lima Pereira L T, Ragni D, Avallone F and Scarano F 2022 Aeroacoustics of sawtooth trailing-edge serrations under aerodynamic loading *J. Sound Vib.* **537** 117202

Liu T, Burner A W, Jones T W and Barrows D A 2012 Photogrammetric techniques for aerospace applications *Prog. Aerosp. Sci.* **54** 1–58
Mendelson L and Techet A H 2018 Multi-camera volumetric PIV for the study of jumping fish *Exp. Fluids* **59** 10
Mertens C, Fernández J L C, Sodja J, Sciacchitano A and Van Oudheusden B W 2023 Nonintrusive experimental aeroelastic analysis of a highly flexible wing *AIAA J.* **61** 3062–77
Mitrotta M A, Sodja J and Sciacchitano A 2022 On the combined flow and structural measurements via robotic volumetric PTV *Meas. Sci. Technol.* **33**
Möller T and Trumbore B 1997 Fast, minimum storage ray-triangle intersection *J. Graph. Tools* **2** 21–28
Pan B 2018 Digital image correlation for surface deformation measurement: historical developments, recent advances and future goals *Meas. Sci. Technol.* **29** 082001
Pappa R S, Black J T, Blandino J R, Jones T W, Danehy P M and Dorrington A A 2003 Dot-projection photogrammetry and videogrammetry of gossamer space structures *J. Spacecr. Rockets* **40** 858–67
Pomerleau F, Colas F, Siegwart R and Magnenat S 2013 Comparing ICP variants on real-world data sets: open-source library and experimental protocol *Auton. Robot.* **34** 133–48
Rusinkiewicz S and Levoy M 2001 Efficient variants of the ICP algorithm *Third Int. Conf. on 3-D Digital Imaging and Modeling* pp 145–52
Saiti E and Theoharis T 2020 An application independent review of multimodal 3D registration methods *Comput. Graph.* **91** 153–78
Saiz G G, Sciacchitano A and Scarano F 2022 On the closure of Collar's triangle by optical diagnostics *Exp. Fluids* **63** 128
Schanz D, Gesemann S and Schröder A 2016 Shake-The-Box: Lagrangian particle tracking at high particle image densities *Exp. Fluids* **57** 1–27
Schanz D, Gesemann S, Schröder A, Wieneke B and Novara M 2013 Non-uniform optical transfer functions in particle imaging: calibration and application to tomographic reconstruction *Meas. Sci. Technol.* **24** 024009
Schröder A and Schanz D 2023 3D Lagrangian particle tracking in fluid mechanics *Annu. Rev. Fluid Mech.* **55** 511–40
Schröder A, Schanz D, Bosbach J, Novara M, Geisler R, Agocs J and Kohl A 2022 Large-scale volumetric flow studies on transport of aerosol particles using a breathing human model with and without face protections *Phys. Fluids* **34** 035133
Segal A V, Haehnel D and Thrun S 2009 *Generalized-ICP Robot.: Sci. Syst* **2** 435 RSS.2009.V.021
Wieneke B 2008 Volume self-calibration for 3D particle image velocimetry *Exp. Fluids* **45** 549–56
Wieneke B 2013 Iterative reconstruction of volumetric particle distribution *Meas. Sci. Technol.* **24** 024008
Wieneke B and Rockstroh T 2024 Lagrangian particle tracking in the presence of obstructing objects *Meas. Sci. Technol.* **35** 055303
Zhang P, Peterson S D and Porfiri M 2019 Combined particle image velocimetry/digital image correlation for load estimation *Exp. Therm Fluid Sci.* **100** 207–21
Zhou Q-Y, Park J and Koltun V 2018 Open3D: a modern library for 3d data processing (arXiv:1801.09847)